Discovering ferro- and piezoelectricity in lead-free oxyhydrides Ln_2H_4O (Ln = Y, La)

Aleksandr Pishtshev[1] | **Evgenii Strugovshcvhikov[1]**

[1]Institute of Physics, University of Tartu, 50411 Tartu, Estonia

Correspondence
Dr. Aleksandr Pishtshev, Institute of Physics, University of Tartu, 50411 Tartu, Estonia
Email: aleksandr.pishtshev@ut.ee

Funding information

One of the most significant aspects of crystal chemistry of multianionic oxyhydrides is the possibility of flexible regulation of the composition-structure-function relationships. In the context of competitive coordinations of different anions in the crystal lattice, this may afford formation of a number of stable stoichiometric phases without inversion symmetry. In the present work, we demonstrated that semiconducting yttrium and lantanium oxyhydrides with the composition Ln_2H_4O (Ln=Y, La) have an attractive potential for the design of novel lead-free ferro- and piezoelectric systems. By means of advanced DFT-based computational simulations we predicted that several polar monoclinic and orthorhombic phases of Ln_2H_4O may exhibit exceptional ferro- and piezoelectric properties as well as electromechanical coupling characteristics that are especially suitable for the piezoelectric devices working in a shear mode. Structure-dependent theoretical evaluations of the relevant physical responses demonstrated estimates of ferro- and piezoelectric characteristics that are comparable with the specifications of advanced ferroelectric solid solutions. Thus, our prediction of lead-free piezoelectric systems forms a solid and technologically reliable basis for the future development of effective and non-hazardous materials.

1 | INTRODUCTION

Ferro- and piezoelectric systems relating to the commercially successful group of functional materials are widely used in numerous technological and scientific applications. The higher level of environmental and medical standards demands the design and development of modern materials with a composition that contains no chemical agents capable of causing any harm to plants, living objects, or natural resources. In this context, the potential of lead-free mixed-anion compounds which exhibit relevant structural/chemical modifications might be attractive for the development of various advanced applications in condensed matter physics, solid-state chemistry, mechano-, piezo- and optoelectronics, and nonlinear optics. If the anionic subsystem is formed by the interplay of hydrogen and oxygen ions, these materials belong to a class of mixed-anion systems called oxyhydrides [1, 2, 3, 4]. Research work on how oxygen and hydrogen anions are sharing the common chemical space in a hydride lattice has been started in the 1990s, when for the first time the bulk titanium and zirconium oxyhydrides Ti/ZrH_xO_y of the different compositions were synthesized and investigated[5, 6]. The central issue of how oxygen as an oxidant triggers a number of functional transformations in transition-metal hydrides became a center of attention of several investigations (a short review can be found in [7]).

Bulk yttrium and lanthanum oxyhydrides are the main object of the present work. The successful synthesis of stable phases of the $Y-H-O$ systems [8, 9, 10] as well as of several rare-earth oxyhydrides [11] raised a principal issue concerning the key factors that govern the formation routes and give rise to structural features of these materials. So far, most of previous studies were limited to experimental research on the synthesis methods and characterizations, and therefore, leaved unexplored the detail description of anionic configurations. To understand the chemistry of partial oxydation processes at the microscopic level, to predict the possible crystallization pathways in terms of the O/H ratio, and to characterize the effect of varying oxygen content on the phase stability and structural properties we performed theoretical work on compositional and structural modeling of the yttrium-hydrogen system mixed with oxygen [12, 13, 14]. Comparison of structural modifications of yttrium oxyhydrides showed that a greater affinity of elemental yttrium for oxygen provides chemical diversity of the predicted phases via the flexible linkage of hydrogen and oxygen anionic sublattices, while the cation sublattice composed solely of Y^{3+} ions forms the rigid crystalline framework. Modeling the amount of the incorporated oxygen, we developed the ternary phase diagram of yttrium oxyhydrides for a wide range of the O/H stoichiometry. In the context of material design, we revealed and explained the ability of metal-hydrogen-oxygen system to straightforwardly crystallize in a ground state whose nature depends on the oxygen content. Also, within the compositional contour, we described the stability limits which involved a number of various composition-dependent crystalline architectures. The key result we obtained in our studies is that the most of condensed phases of different stoichiometries presented in the phase diagram can be mainly grouped into two homologous series, $Y_{(2n+m)/3}H_mO_n$ and $Y_{(4n+2m)/5}H_mO_n$. We showed that the attractive point of these materials is a set of composition-structure-property relationships which may be encoded in structural transformations: that is, the flexibility of layered anion configurations ensures the possibility of several options for stabilization of an oxyhydride architecture. In view of the experimental situation, this implies that material functions may be governed by structural relationships in the system. Important aspect here is that the dynamic stability of a lattice geometry is kept by the proper distribution of anions within the rigid metal (cation) sublattice. The induced difference of local charge density patterns may cause cationic and anionic displacements that can break inversion symmetry of the crystal lattice.

The possibility of crystal structures with polar phases for the second $n = 1$, $m = 4$ member of the $Y_{(2n+m)/3}H_mO_n$-type family was already considered in our previous work [13]. It is worth noting that especially important in the context of loss of a symmetry center is a perfect stoichiometry because owing to soft chemistry of anion exchanges the lattice stability of the bulk oxyhydride system is governed by macroscopic charge redistribution which strongly depends on how the oxygen and hydrogen subsystems share valence charge density. This provides the structural/topological variability

of the bulk versions of the 2:4:1 stoichiometry which due to the emergence of polar distortions in the crystal lattice may give rise to a wide functionality of dielectric behaviour in response to external mechanical stress or electric field. Thus, the main purpose of the present theoretical work is (i) to systematically investigate the piezo- and ferroelectric properties of Ln_2H_4O (Ln = Y, La) crystalline systems, (ii) to understand how the interplay of anionic degrees of freedom may control functionality of the material via its structural non-centrosymmetricity, and (iii) to propose a new generation of stable polar phases of lead-free oxyhydride compounds with enhanced dielectric properties.

2 | RESULTS AND DISCUSSION

2.1 | Layered oxyhydrides Ln_2H_4O (Ln = Y, La)

In Ref. [13], we determined the composition range and limits of the general stability for solid phases in which the Y-H-O system may be condensed. As a key result, we suggested the composition-structure phase diagram which embraced a number of energetically and structurally stable phases and compounds. Based on our previous study, we chose the ternary composition with stoichiometric oxygen content O/H = 1/4 because it may crystallize to lattice geometries described by non-centrosymmetric space groups. To test the isostructural tendency with respect to La cation and to examine the substitution effect we performed DFT-based simulations of lanthanum based oxyhydrides by considering the full Y-site isomorphous substitution in non-centrosymmetric modifications of the bulk Y_2H_4O. The optimized
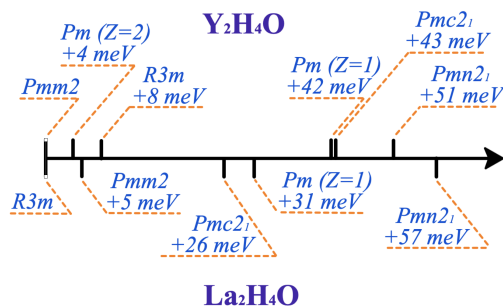

FIGURE 1 Comparison of energetics (per atom) of different crystalline phases of Table 1. Zero point corresponds to the most stable structure.

geometries along with the validation of relative thermodynamic stability are presented in Table 1 in terms of comparison of equilibrium lattice parameters and energetics for isostructural yttrium and lanthanum based oxyhydrides. We also added new phases to this table. Note that no imaginary frequencies that might emerge in the Γ point have been found in all the systems. In addition, we represented graphically benchmark evaluations of energetics in Figure 1. Each point here is specified by its distance from the reference point which corresponds to the most stable structure.

As seen from Table 1, the $Pmm2$ polar phase is the most energetically favorable among all the modifications of yttrium oxyhydrides we predicted for the Y_2H_4O composition; all of them, in addition to structural stability, demonstrate thermodynamic one with respect to decomposition scenarios. However, the combination with La cation in the given phase indicates small thermodynamic instability with respect to the possible decomposition into more simple oxyhydride LaHO and binary oxide La_2O_3. More details on crystallographic data and structural stability are provided in Tables S1–S11 and S12 of Supporting Information (SI). Discussion on crystallographic properties of the crystalline phases

TABLE 1 Comparison of equilibrium parameters of crystal structure and energetics for Ln_2H_4O (Ln = Y, La) compounds. Structural data for the Pm, $Pmn2_1$ and $R3m$ lattice geometries of Y_2H_4O (marked with asterisk) were calculated in Ref. [13]. The energetics is represented in terms of three different decomposition schemes (ΔH, ΔE_1, and ΔE_2). The last column reflects relative differences of the Madelung contribution (ΔW_M) into the lattice energy.

Chem.	Space	Phase	Z	Lattice constants (Å)			V	Density	ΔH	ΔE_1	ΔE_2	ΔW_M
formula	symm.	type	(f.u.)	a	b	c	(Å³)	(g/cm³)	(kJ/mol)	(kJ/mol)	(kJ/mol)	(kJ/mol)
Y_2H_4O*	Pm	mono-	1	3.677	3.724	5.409	74.00	4.44	−847.4	−58.9	−25.9	+36
	(6)	clinic			$\beta = 92.35°$							
La_2H_4O				3.934	4.021	5.821	92.06	5.37	−799.2	+5.2	+21.9	+33
					$\beta = 91.22°$							
Y_2H_4O	Pm	mono-	2	6.439	3.669	6.599	148.02	4.44	−872.9	−84.4	−51.3	+7
	(6)	clinic			$\beta = 108.30°$							
Y_2H_4O	$Pmm2$	ortho-	2	3.628	7.648	5.396	149.72	4.39	−875.6	−87.1	−54.1	0
	(25)	rhombic										
La_2H_4O				3.958	8.067	5.831	186.18	5.31	−816.3	−11.8	+4.8	+11
Y_2H_4O	$Pmc2_1$	ortho-	2	3.726	3.674	10.808	147.95	4.44	−847.3	−58.8	−25.7	+36
	(26)	rhombic										
La_2H_4O				4.022	3.936	11.637	184.22	5.37	−802.2	+2.3	+18.9	+33
Y_2H_4O*	$Pmn2_1$	ortho-	2	3.606	6.453	6.519	151.69	4.33	−841.2	−52.7	−19.7	+16
	(31)	rhombic										
La_2H_4O				3.923	6.949	6.905	188.24	5.25	−781.1	+23.3	+40.0	+24
Y_2H_4O*	$R3m$	tri-	3	3.676	3.676	18.542	216.99	4.54	−870.1	−81.7	−48.6	+2
	(160)	gonal										
La_2H_4O				3.983	3.983	19.778	271.68	5.46	−819.8	−15.4	+1.2	0

The quantity ΔH denotes the enthalpy difference which corresponds to the energetics of decomposition reaction into Ln, $\frac{1}{2}H_2$, and $\frac{1}{2}O_2$. The quantities ΔE_1 and ΔE_2 indicate the calculated formation energy which corresponds to the energetics of reaction on decomposition into (i) most stable oxide (Ln_2O_3) and trihydride (LnH_3), or (ii) the half-and-half mixture of LnHO and LnH_3, respectively. The estimates of the Madelung contribution ΔW_M, −6528 and −6045 kJ/mol, have been taken as the reference points for the $Pmm2$ structure of Y_2H_4O and the $R3m$ structure of La_2H_4O, respectively.

of Ln_2H_4O (Ln = Y, La) can be found in Section 4. Here, we note several distinctive structural features. In Figure 2a we depict the triangular layered structure described by $R3m$ space group. The lattice geometry is that of the IIIa polytypic form of $ZnIn_2S_4$ system [15, 16]. The structure may be referred to a trigonally distorted close-packed atomic arrangement in which all the O atoms and half of the Ln atoms occupy tetrahedral holes, while the other half of Ln atoms prefer octahedral holes. In the crystal class $mm2$ we identified three different orthorhombically-distorted lattice geometries with symmetry isomorphic to polar point group C_{2v} (Table 1). The most important factor of their
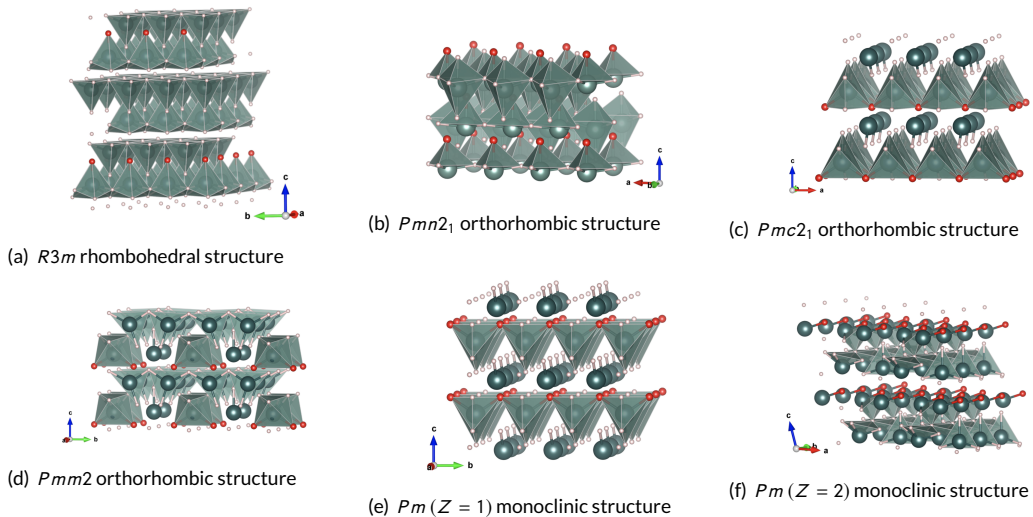
(a) $R3m$ rhombohedral structure

(b) $Pmn2_1$ orthorhombic structure

(c) $Pmc2_1$ orthorhombic structure

(d) $Pmm2$ orthorhombic structure

(e) Pm ($Z = 1$) monoclinic structure

(f) Pm ($Z = 2$) monoclinic structure

FIGURE 2   A perspective view of the layered topology of ternary Ln_2H_4O (Ln = Y, La) oxyhydride systems (Table 1) in terms of the polyhedral representations. Ln, O and H atoms are drawn in dark green, red and pink, respectively.

architecture is layered topology of the crystal lattice. The structures are characterized by the asymmetric coupling of atomic displacements which in turn forms three-dimensional non-centrosymmetric patterns with a sublattice polar ordering. The latter gives rise to such macroscopic effects as spontaneous electric polarization and piezoelectricity. The equilibrium structures of these orthorhombic systems are illustrated in Figure 2. In particular, Figure 2b shows the $Pmn2_1$ polar structure composed of double layers of anion-centred corner-sharing OLn_4 tetrahedra along with a condensed set of LnH_6 polyhedra. The ordering is realized via alternation of the layers along the b axis. The $Pmc2_1$ structure indicated in Figure 2c represents the other modification of layered geometry: the layers being stacked along the c axis are separated by condensed tetrahedral-type LnH_3O units joined with infinite hydrogen chains. By sharing common corner hydrogen atom the LnH_3O units are linked into infinite isolated chains extended along the a axis. The third possibility for crystallization of Ln_2H_4O is given by the polar orthorhombic system with the space group $Pmm2$ (Figure 2d). This modification represents a framework of edge-sharing polyhedra which is formed by the layers composed of negatively charged $2(LnH_2O)^{-1}$ and positively charged $2(LnH_2)^{+1}$ polyhedral combinations. The effect of monoclinic distortion of an orthogonal Ln_2H_4O system lowers the lattice symmetry towards space group Pm. In Figures 2e and 2f we compare both monoclinic phases with $Z = 1$ and $Z = 2$, respectively. Importantly, these structures differ not only by the number of formula units per the unit cell, but also by the change of the architecture of Y–O and Y–H linkages in passing to $Z = 2$. That is, a certain loss of simplicity associated with the characteristic alternation of the yttrium-oxygen and yttrium-hydrogen slices changes the simple monoclinic structure with $Z = 1$ to more complicated form of the layered architecture which stacks additional atomic planes but retains a common topology of the crystal ordering with the Pm symmetry.

Description of elastic and aggregate properties evaluated by means of the elasticity theory (bulk, Young's and shear moduli, Poisson's ratio) as well as estimates of Grünaisen parameter, Debay's temperature, and Vickers hardness are summarized in Table 2. A result of the full cation substitution Y→La in the Y_2H_4O composition shows that phases of lanthanum oxyhydride are softer and have lower hardness (H_V) than their unsubstituted counterparts. The other important observation from Table 1 is that thermodynamic stability of La_2H_4O crystallization is much reduced as

TABLE 2 Macroscopic elastic and aggregate properties evaluated for Ln_2H_4O crystal phases.

Chem.	Structure	B	E	G	G/B	v	γ	Θ_D	H_V
Y_2H_4O	Pm ($Z = 2$)	89.2	153.9	63.5	0.71	0.21	1.88	567	12.2/11.8
	$Pmm2$	93.5	137.4	54.8	0.59	0.25	2.60	530	8.1/8.5
	$Pmc2_1$	79.6	130.8	53.3	0.67	0.23	2.08	520	9.8/9.8
Y_2H_4O[a]	Pm ($Z = 1$)	78.7	127.3	51.7	0.66	0.23	2.15	513	9.3/9.3
	$Pmn2_1$	91.1	136.1	54.4	0.60	0.25	2.52	529	8.3/8.7
	$R3m$	96.1	151.7	61.3	0.64	0.24	2.26	557	10.1/10.2
La_2H_4O	Pm ($Z = 1$)	72.0	101.7	40.2	0.56	0.26	2.81	384	5.8/6.5
	$Pmm2$	76.3	113.9	45.5	0.60	0.25	2.52	408	7.2/7.6
	$Pmc2_1$	71.5	102.5	40.6	0.57	0.26	2.74	385	6.0/6.7
	$Pmn2_1$	62.9	93.7	37.4	0.59	0.25	2.54	371	6.1/6.6
	$R3m$	82.6	114.1	44.9	0.54	0.27	2.94	405	6.1/6.8

Bulk (B), Young's (E), shear (G) moduli, and Vickers hardness (H_V) are given in GPa, Debye temperature (Θ_D) – in K; v and γ denote the estimates of Poisson's ratio and Grünaisen parameter, respectively.

[a] For comparison we quoted the characteristics obtained in [13].

compared to Y_2H_4O. This implies that partial combination of Y and La site occupations may provide the ground state that becomes energetically less favourable with respect to possible chemical decomposition. Moreover, one can expect that the most structures of the bulk La_2H_4O (with the only exception of $R3m$ phase) may be available as metastable crystalline phases.

2.2 | Ferroelectric order in polar phases of Ln_2H_4O

To evaluate ferroelectric properties we performed accurate calculations of nonzero components of macroscopic dielectric tensor and macroscopic electric polarization. Table 3 summarizes possible polar orderings in terms of the trigonal, orthorhombic, and monoclinic symmetries along with the indication of relevant prototype phases relating to a reference high-symmetry structure. For these prototypes (given below in Table 7 of Section 4) we prescribed the corresponding distortion mode (the primary symmetry mode accompanied the structural transformation) along which the high-symmetry structure is distorted in order to stabilize the crystal lattice in the ferroelectric (or pyroelectric) phase. The details of calculations are listed in Table S13 of SI. In particular, on can see that in the case of strong ferroelectric the ionic and electronic contributions to the electric polarization P_s have equal signs, and the electronic contribution substantially outweighs the ionic one.

Comparison with the data gathered in Ref. [20] indicates that the most of polar phases of Table 3 exhibit a spontaneous polarization that falls into the the range typical for generic ferroelectric materials. Moreover, factors of acentric configuration belonging to both monoclinic modifications are almost ideal for establishing the long-range ferroelectric

TABLE 3 Dielectric characteristics evaluated for polar phases of Ln_2H_4O. In the last column, the nature of the ground state is specified either as ferroelectric (F) or as pyroelectric (P).

Phase	Comp.	E_g (eV)	ϵ	P_s ($\mu C/cm^2$)		Reversible	Prototype	Distortion	
				c	a	Y/N	phase	mode	F/P
Pm	Y_2H_4O	1.8	25.2	3.7	81.8	Y	$P\text{-}4m2$	Γ_5	F
($Z=1$)	La_2H_4O	2.2	29.2	3.3	3.2	Y			F
Pm	Y_2H_4O	2.4	19.8	5.4	75.2	Y	$P2_1/m$	Γ_3 [a)]	F
$Pmm2$	Y_2H_4O	2.8	25.1	4.1	–	Y	$Cmc2_1$	$Y_4 \oplus \Gamma_1$ [b)]	F
	La_2H_4O	2.6	29.0	3.7	–	Y			F
$Pmc2_1$	Y_2H_4O	1.8	26.7	7.4	–	Y	$Amm2$	Y_4	F
	La_2H_4O	2.1	24.6	6.6	–	Y			F
$Pmn2_1$	Y_2H_4O	2.8	15.8	73.0	–	Y	$Pmmn$	Γ_4^-	F
	La_2H_4O	2.7	17.6	4.0	–	Y			F
$R3m$	Y_2H_4O	1.9	28.9	16.8	–	N	$R\text{-}3m$	Γ_2^- [a)]	P
	La_2H_4O	2.4	25.5	14.1	–	N			P

The dielectric gap E_g was modeled in [17] by using HSE06 hybrid functional scheme [18, 19]. Relative dielectric constant ϵ represents the direct average over crystal axes. Components of the electric polarization P_s are given for the polar directions c and a.

[a)] The change to polar structure is associated with a reconstructive phase transformation.

[b)] The transitional path proceeds via the intermediate phase $Pca2_1$ as follows: $Cmc2_1 \rightarrow Pca2_1$ with index 2 and $Pca2_1 \rightarrow Pmm2$ with index 4.

order. In particular, in-plane components of the macroscopic polarization reach values that are very close to those exhibiting such canonical systems as $PbTiO_3$, $BaTiO_3$ and $LiNbO_3$. The other fascinating record of Table 3 are the cases of the $P2_1/m$ to Pm and $R\text{-}3m$ to $R3m$ symmetry-breaking distortions that proceed in the scheme of reconstructive transition but do not change the crystal system. Obviously, the reason why both configurations undergoes the further symmetry-lowering is that atoms accommodated on the mirror plains remain stereochemically active in nonpolar phase. Note also that although the symmetry of the $R3m$ trigonal structure permits the ferroelectric ordering, the numerical estimates which indicated the amplitude of the polarization vector at zero temperature about $16.8\,\mu C/cm^2$ showed that no reversible crystal polarization occurs along the admissible direction – polar c-axis. Therefore, one should consider the $R3m$ phase as having pyroelectric nature.

2.3 | Piezoelectric properties and structural features

By simulating the electric responses to deformation we evaluated the strain-induced piezopotential and analyzed the bulk piezoelectric activity of Ln_2H_4O. The main piezoelectric characteristics we obtained in our calculations are summarized in Table 4 for all the predicted polar phases. One can emphasize that regardless of the fact that oxyhydride compounds in the condensed form are considerably dense (Table 2), the interplay of electric and elastic responses in polar anisotropic medium may be greatly effective to the piezoelectric sensitivity. The key result which follows from the comparison with data of Table S14 of SI is that the most of the bulk oxyhydride structures exhibit enhanced

TABLE 4 Summary of piezoelectric and elastic responses presented in terms of piezoelectric stress e_{ij} and strain d_{ij} tensors along with elastic constants C_{ij}.

Struct.	Comp.	C_{11}	C_{12}	C_{13}	C_{15}	C_{22}	C_{23}	C_{25}	C_{33}	C_{35}	C_{44}	C_{46}	C_{55}	C_{66}
$Pm\,(Z=1)$	Y_2H_4O	128.4	41.0	40.5	−36.8	197.3	63.4	3.4	168.1	−8.1	74.6	−12.2	54.0	40.6
	La_2H_4O	111.2	24.5	50.8	−29.8	168.5	62.6	3.8	132.2	−0.3	62.9	−3.9	40.7	28.2
$Pm\,(Z=2)$	Y_2H_4O	176.8	57.9	36.4	0.7	206.3	38.4	−17.0	165.4	−7.1	62.6	−11.8	53.7	68.6

Struct.	Comp.	e_{11}	e_{12}	e_{13}	e_{15}	e_{24}	e_{26}	e_{31}	e_{32}	e_{33}	e_{35}
$Pm\,(Z=1)$	Y_2H_4O	2.51	0.04	0.55	0.87	1.48	1.42	−0.01	0.27	0.52	0.55
	La_2H_4O	3.20	0.22	0.47	1.63	1.18	0.62	−0.35	0.24	0.26	0.18
$Pm\,(Z=2)$	Y_2H_4O	0.93	0.07	0.54	0.37	0.28	0.12	0.69	0.60	1.21	0.29

Struct.	Comp.	d_{11}	d_{12}	d_{13}	d_{15}	d_{24}	d_{26}	d_{31}	d_{32}	d_{33}	d_{35}	d_{15}/d_{11}	d_{15}/d_{33}
$Pm\,(Z=1)$	Y_2H_4O	33.25	−7.4	−0.05	39.6	26.8	43.0	2.7	−0.4	3.2	12.6	1.19	12.38
	La_2H_4O	60.2	−2.6	−18.1	84.2	20.3	24.8	−4.6	0.8	3.3	1.02	1.40	25.5
$Pm\,(Z=2)$	Y_2H_4O	5.0	−1.0	2.66	6.76	4.9	2.58	1.9	1.65	6.79	6.72	1.35	0.995

Struct.	Comp.	C_{11}	C_{12}	C_{13}	C_{22}	C_{23}	C_{33}	C_{44}	C_{55}	C_{66}
$Pmm2$	Y_2H_4O	205.3	44.5	68.4	137.3	55.8	176.9	41.9	67.2	53.0
	La_2H_4O	169.8	25.7	61.8	114.6	52.3	135.6	46.2	61.1	34.8
$Pmc2_1$	Y_2H_4O	197.0	43.7	64.0	104.7	35.1	166.2	54.0	74.8	38.7
	La_2H_4O	168.2	27.2	62.4	92.2	50.5	131.2	40.1	62.9	28.2
$Pmn2_1$	Y_2H_4O	185.8	55.6	38.6	205.0	43.3	161.1	50.3	29.3	70.0
	La_2H_4O	143.4	51.2	23.5	138.9	22.4	103.9	31.1	23.2	45.0

Struct.	Comp.	e_{15}	e_{24}	e_{31}	e_{32}	e_{33}		d_{15}	d_{24}	d_{31}	d_{32}	d_{33}	d_{15}/d_{33}
$Pmm2$	Y_2H_4O	0.93	0.95	0.04	0.36	0.17		13.8	22.7	−0.5	2.6	0.3	46
	La_2H_4O	0.53	−0.80	−0.08	−0.01	−0.38		8.7	−17.4	0.6	1.5	−3.7	−2.35
$Pmc2_1$	Y_2H_4O	1.66	1.14	0.26	0.33	0.57		22.2	21.0	−0.1	2.2	3.0	7.4
	La_2H_4O	1.12	0.68	0.22	−0.19	0.27		17.7	17.0	0.8	−4.1	3.3	5.36
$Pmn2_1$	Y_2H_4O	0.92	0.65	0.02	0.42	0.84		31.4	12.9	−1.4	1.4	5.2	6.04
	La_2H_4O	0.96	0.86	0.28	1.10	1.49		41.1	27.7	−2.7	6.7	13.5	3.04

Struct.	Comp.	C_{11}	C_{12}	C_{13}	C_{14}	C_{33}	C_{44}	C_{66}
$R3m$	Y_2H_4O	206.3	73.3	33.3	−22.5	181.3	56.0	66.5
	La_2H_4O	164.8	59.8	32.7	−21.6	165.0	39.5	52.5

	Comp.	e_{15}	e_{22}	e_{31}	e_{33}		d_{15}	d_{16}	d_{22}	d_{31}	d_{33}	d_{15}/d_{33}
	Y_2H_4O	−0.72	−0.43	−0.50	−1.70		−11.7	2.0	−1.0	−0.7	−9.2	1.27
	La_2H_4O	−0.43	0.22	−0.12	−1.44		−17.0	−11.2	5.6	0.8	−9.0	1.89

Symmetry-allowed nonzero components of e_{ij}, d_{ij}, and C_{ij} are given in C/m², pC/N, and GPa, respectively.

piezoelectricity associated with the shear mode. As seen from Table 4, there exist both in-plane and out-of-plane piezoelectric responses with the ratio (displayed in terms of d_{15}/d_{33} and d_{15}/d_{11}) differing by an order of magnitude. This indicates the large shear-mode piezoelectric effect [21, 22, 23]. Since variations of the piezoelectric anisotropy can be attributed to wide flexibility of the multilayer-structured architectures of Ln_2H_4O (Table 1 and Tables S1–S11 of SI), a core feature of the geometry of strain or displacive distortions is that the powerful increase of the piezoelectric effect is associated with the large enhancement of shear components d_{15} and d_{24} of the piezoelectric strain tensor. Our estimates of d_{15} and d_{24} which are comparable with those exhibiting by advanced piezoelectric systems [24, 25, 26, 27] show that greatly enhanced piezoelectric responses governed by the low-symmetry Pm monoclinic phase of Ln_2H_4O utilize two intrinsic structural factors: the regular shear (d_{15}) and in-plane axial strain (d_{11}). On the other hand, no visible enhancement of the longitudinal and radial contributions to piezoelectric properties has been observed in our calculations. In the context of d_{33} and d_{31} coefficients, our results demonstrate no essential difference as compared with the typical values of d_{33} and d_{31}, 11.7 and -5.5 pC/N, respectively, known for ZnO-type semiconductor [28, 29]. Note that materials demonstrating a high level of piezoelectric anisotropy are of special interest to the design of such devices as actuators and transducers [23] as well as to the development of applications for the energy harvesting [21, 30].

Before we consider the features of electromechanical coupling we should emphasize the importance of correlation between acentric character of the lattice geometry and valence charge distribution for piezo-activity of the oxyhydride system. The modeling and design of PZT-type (lead zirconate titanate) systems provide a good example of how the direct coupling of mechanical and charge degrees of freedom may be further enhanced by compositional tailoring of macroscopic polarity of the ferroelectric medium [23, 27, 31]. This is typically achieved via the site engineering by driving the interplay between local lowering of symmetry caused by distortions of microstructure and local redistribution of internal electric charges in a multi-component relaxor-perovskite-based solid solution. For comparison, the controlling mechanism of a high piezoelectric activity in the Ln_2H_4O crystalline system is entirely different, in the sense that the site engineering deals with the factors stipulated by the multianion character of the chemical composition. Our first-principles analysis showed that the electric strength generated by the volatile distribution of internal electric field patterns governs the sensitivity of the piezoelectric effect. This is caused by the original force geometry within the anion subsystem in which both directional and non-directional charge distortions are subjected to short-range interactions. This effect is a direct consequence of the specific functionality of the oxyhydride crystal lattice – an electronic hardness which being determined by a spatial distribution of anion positions is responsible for the balance between long-range and short-range forces [12, 13]. Due to the dynamic nature of such balance [32], provided by the tough interplay of electron and lattice contributions, even small deformations of asymmetric configuration may substantially strengthen charge fluctuations that in turn will induce strong internal electric fields, making thus the system more sensitive to a response effect. This implies that by governing the electronic hardness dependence on the structure features one can gain control over the effective conversion of the piezoelectric energy. We highlighted this important fact in Table 5 where we characterized electro- and acousto-mechanical properties for the Ln_2H_4O piezo-active phases that may be appropriate for the use in ultrasonic and energy-harvesting applications (which are mainly based on the utilization of the piezoelectric shear mode) [21, 23, 30, 33, 31, 34, 35]. In particular, comparison performed in terms of shear oscillations (d_{15}, k_{15}, g_{15}) showed that these phases exhibit electromechanical couplings similar to electromechanical shear constants of PZT-type materials. Moreover, in the context of a piezoactuator device it is worthwhile to note that the Young's moduli listed in Table 2 exhibit values that along with the ability of the internal force/displacement generation may serve as a sound indicator of the possibility to reach a high actuator stiffness. Table 6 illustrates how lowering space symmetry to monoclinic one extends the strength of electromechanical connections. For instance, one can see that both monoclinic Ln_2H_4O systems exhibit in-plane axial (d_{11}, k_{11}, g_{11}) piezoelectric coefficients well comparable with the longitudinal constant d_{33} of the advanced piezoceramics [26, 36].

TABLE 5 Coupling between electric and mechanical fields in the Ln_2H_4O phases with high piezoelectric response.

Phase	ϵ_{11}	d_{15}	S_{55}	k_{15}	d_{31}	S_{11}	k_{31}	ϵ_{33}	d_{33}	S_{33}	k_{33}	g_{15}	g_{31}	g_{33}	$d_{15}\cdot g_{15}$	$d_{31}\cdot g_{31}$	$d_{33}\cdot g_{33}$
Y_2H_4O																	
Pm ($Z=1$)	20.45	39.6	23.71	60%	2.7	11.02	6%	20.61	3.2	7.07	9%	218.8	14.8	17.5	8670	40	60
Pm ($Z=2$)	17.59	6.76	19.26	12%	1.9	6.42	6%	20.88	6.79	6.50	20%	43.4	10.3	36.7	290	20	250
$Pmm2$	21.46	13.8	14.88	26%	0.5	5.73	2%	13.62	0.3	7.10	1%	72.7	4.1	2.5	1000	2	1
$Pmc2_1$	37.46	22.2	13.36	33%	0.1	6.14	0.3%	19.87	3.0	7.10	8%	67.0	0.6	17.1	1490	1	50
$Pmn2_1$	17.15	31.4	34.15	44%	1.4	6.02	5%	12.74	5.2	6.77	19%	206.9	12.4	46.1	6500	20	240
$R3m$	31.26	11.7	20.67	15%	0.7	6.22	2%	24.09	9.2	5.77	26%	42.3	3.3	43.2	490	2	400
La_2H_4O																	
Pm ($Z=1$)	35.26	84.2	32.26	84%	4.6	14.28	9%	21.74	3.3	11.15	7%	269.8	23.9	17.2	22720	110	60
$Pmm2$	29.64	8.7	16.35	13%	0.6	7.06	2%	16.65	3.7	10.37	9%	33.2	4.1	25.1	290	2	90
$Pmc2_1$	30.76	17.7	15.90	27%	0.8	7.23	2%	21.48	3.3	11.17	7%	65.0	4.2	17.4	1150	3	60
$Pmn2_1$	18.46	41.1	43.03	49%	2.7	8.18	8%	16.28	13.5	10.16	35%	251.6	18.7	93.7	10340	50	1270
$R3m$	26.43	17.0	32.60	19%	0.8	8.50	2%	23.76	9.0	6.43	24%	72.7	3.8	42.8	1240	3	390

Comparison of electro- and acousto-mechanical properties utilizes the components of the macroscopic dielectric ϵ_{ij} (relative permittivity), piezoelectric strain d_{ij} (piezo modulus, pC/N), and elastic compliance S_{ij} (TPa^{-1}) tensors taken in polarization directions. The energy harvesting performance is characterized in terms of electromechanical coupling coefficients k_{ij}, piezoelectric voltage constants g_{ij} ($10^{-3}\times$[Vm/N]), and transduction coefficients $d_{ij}\cdot g_{ij}$ ($10^{-15}\times$[m^2/N]).

TABLE 6 Effect of monoclinic distortion on electromechanical characteristics.

Phase	d_{11}	k_{11}	ϵ_{22}	d_{26}	S_{66}	k_{26}	g_{11}	g_{26}	$d_{11}\cdot g_{11}$	$d_{26}\cdot g_{26}$
Y_2H_4O										
Pm ($Z=1$)	33.25	74%	34.58	43.0	25.93	48%	183.7	140.5	6108	6042
La_2H_4O										
Pm ($Z=1$)	60.2	90%	30.67	24.8	35.77	25%	192.9	91.4	11613	2267

It is further interesting to highlight that for all polar phases the shear piezoelectric coefficient d_{15} is much larger than the longitudinal d_{33} and transverse d_{31} ones (Table 5). This fact correlates well with the inequality relation $d_{31}<d_{33}<<d_{15}$ known for perovskite-type ferroelectric crystals [37]. Character of movements of the oxygen octahedron which only rotates with ease in the perovskite structure as compared with stretch or squeeze deformations is usually applied to the explanation of such difference [31]. In the case of the Ln_2H_4O oxyhydride, two key factors give the understanding why the system exhibits much better piezoelectric properties in the shear mode than in the longitudinal or transverse ones. The first factor stems from the layered structure in which the 2:4:1 chemical composition crystallizes. Polar phases of different symmetries (Table 1) can be considered as stable configurations of highly-oriented structural motifs. The corresponding analysis of the relevant vibrational and elastic degrees of freedom indicated that lattice changes are mainly caused by the coupling of atomic displacements between the layers while the intralayer movements proceed relatively easier. This feature of layer topology stipulates the role of the other factor – the flexibility of rotations of

anionic polyhedra. As an illustration of the interrelation between the elastic anisotropy and piezoelectric modes (based on the polarization-related electrostriction) we presented in SI Supplementary figures S1 and S2 which for the crystal phase with Pm (Z =1) space symmetry visualize spatial dependencies of the linear compressibility in terms of the shapes of representation surfaces.

3 | CONCLUSION

In this work, we presented a general theoretical perspective of compositionally-simple promising candidates for development of a lead-free ferroelectric and piezoelectric materials based on the Ln_2H_4O (Ln = Y, La) oxyhydride composition. A number of structural distortions subjected to the different interatomic distances in oxygen-hydrogen configurations around Ln^{3+} cation environment have been considered for possible crystallization pathways of the Ln_2H_4O compound. Lattice models of polar phases with appropriate monoclinic, orthorhombic and trigonal crystallographic orientations have been investigated. On the base of first-principles simulations we found clear indications that the lattice stabilization of polar orderings has the electronic nature and is caused by the interplay of anionic charge distributions in the cationic framework. The requirement of the exact 2:4:1 stoichiometry is essential to reach macroscopic stability via establishing the relative balance between long-range and short-range interactions. Results of modeling of the structure-property relationships showed that the oxyhydride polar phases have unexplored and competitive potential for the design of lead-free piezoelectric materials. We investigated the dielectric properties, macroscopic electric polarization, piezoelectric responses, and variation of the electromechanical properties. We found that the high piezoelectric performance of several ferroelectric phases of the bulk Ln_2H_4O is characterized by the piezoelectric-shear-mode strength to elastic properties ratio and by the energy transduction capabilities. This offers a number of attractive advantages for the application of oxyhydrides in the development of piezo-electronics and energy harvesting lead-free devices.

4 | THEORETICAL SECTION: CRYSTAL PHASES, METHODOLOGY

4.1 | $R3m$ trigonal architecture

Equilibrium cell parameters and unit-cell volume for the $R3m$ acentric ordering are given in Table 1. A primitive cell is formed by 7 atoms; each atom occupies a $3a$ site with point symmetry described by two-dimensional group $3m$ (C_{3v}). The layers pattern comprises a stacking sequence H(4) H(3) H(1) Ln(2) H(2) O(1) Ln(1) in which atoms differs by variable z coordinate. The sequence repeats oneself three times in the unit cell. The number of hydrogen layers, N_H = 12, determines the length of the lattice constant c as $N_H \times 1.545$ Å for Y_2H_4O and $N_H \times 1.648$ Å for La_2H_4O, respectively. Figure 3 illustrates the difference of the distribution of Ln^{3+} ions over two interpenetrating triangular-type sublattices. As indicated in Table 1, both systems, Y_2H_4O and La_2H_4O, are thermodynamically stable under the simulated conditions. The evaluation of vibrational properties we have performed on the base of the optimized geometries showed that the $R3m$ crystal geometry is structurally/dynamically stable with respect to atomic/sublattice displacements and mechanical shears. The initial (parent) high-symmetry phase of the bulk Ln_2H_4O can be evaluated via the addition of such extra symmetry element as inversion. The prototype lattice can therefore be conceived as having a similar higher-symmetry R-$3m$ layered motive in which both metal atoms along with all the hydrogen atoms become pairwise-combined into $6c$ orbits that in turn are conjugated to a center of inversion at the origin (0, 0, 0.5) determined by the oxygen $3b$ orbit. Table 7a shows the crystallographic data calculated for the structure of the bulk Y_2H_4O that belongs to the centric space group R-$3m$. The unit cell is illustrated in Figure 4a. No dynamical instability was found

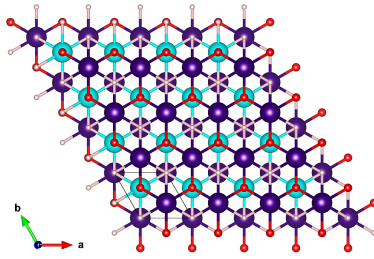**FIGURE 3** Mutual arrangement of two metallic sublattices in the $R3m$ crystal structure of Ln_2H_4O. O and H atoms are drawn in red and pink, respectively; Ln atoms shown in violet and turquoise demonstrate the difference of the sublattices. The point symmetry of the Ln^{3+} $3a$ sites corresponds to two-dimensional trigonal group C_{3v}.

TABLE 7 Crystallographic description of high-symmetry prototype structures in terms of the Bravais lattice for different phases of Y_2H_4O.

Atom	Site	Symm.	x	y	z
Y(1)	6c	3m	0	0	0.2456
O(1)	3b	−3m	0	0	0.5
H(1)	6c	3m	0	0	0.3636
H(2)	6c	3m	0	0	0.0759

(a) The R-$3m$ symmetry. Lattice parameters: 3.562 and 18.733 Å, $\gamma = 120°$.

Atom	Site	Symm.	x	y	z
Y(1)	2a	mm2	0.25	0.25	0.6542
Y(2)	2a	mm2	0.25	0.25	0.1184
O(1)	2b	mm2	0.25	0.75	0.1041
H(1)	4e	m..	0.25	0.5731	0.7904
H(2)	4e	m..	0.25	0.0133	0.3959

(b) The $Pmmn$ symmetry. Lattice parameters: 3.494, 5.354 and 7.488 Å.

Atom	Site	Symm.	x	y	z
Y(1)	2a	mm2	0	0	0.1262
Y(2)	2b	mm2	0.5	0	0.4035
O(1)	2b	mm2	0.5	0	0
H(1)	2a	mm2	0	0	0.5461
H(2)	2b	mm2	0.5	0	0.2213
H(3)	4d	m..	0	0.2360	0.3100

(c) The $Amm2$ symmetry. Lattice parameters: 3.628, 4.179 and 10.940 Å.

Atom	Site	Symm.	x	y	z
Y(1)	4a	m..	0	0.5236	0.1423
Y(2)	4a	m..	0	0.0339	0.1342
Y(3)	8b	1	0.2511	0.2799	0.3767
O(1)	4a	m..	0	0.2658	0.2538
O(2)	4a	m..	0	0.2134	0.7573
H(1)	4a	m..	0	0.4165	0.4509
H(2)	4a	m..	0	0.2702	0
H(3)	8b	1	0.1676	0.0327	0.4688
H(4)	8b	1	0.2600	0.0227	0.2582
H(4)	8b	1	0.2662	0.1906	0.0810

(d) The $Cmc2_1$ symmetry. Lattice parameters: 7.435, 7.483 and 10.853 Å.

Atom	Site	Symm.	x	y	z
Y(1)	2g	2mm.	0	0.5	0.2440
O(1)	1b	−4m2	0.5	0.5	0
H(1)	1d	−4m2	0	0	0.5
H(2)	1a	−4m2	0	0	0
H(3)	2g	2mm.	0	0.5	0.6476

(e) The P-$4m2$ (115) symmetry. Lattice parameters: 3.662 and 5.399 Å.

Atom	Site	Symm.	x	y	z
Y(1)	2e	m	0.4810	0.25	0.2359
Y(2)	2e	m	0.0498	0.25	0.7677
O(1)	2e	m	0.6874	0.25	0.0274
H(1)	2e	m	0.3090	0.25	0.6519
H(2)	2e	m	0.9219	0.25	0.4146
H(3)	2e	m	0.6464	0.25	0.6057
H(4)	2e	m	0.1167	0.25	0.1421

(f) The $P2_1/m$ symmetry. Lattice parameters: 6.622, 3.447 and 6.641 Å, $\beta = 112.11°$.

both in the ferroelastic and ferroelectric channels for this modification. Therefore, a possible relationship between these phases in the context of the driving force for the R-$3m \rightarrow R3m$ evolution can be related to a reconstructive transformation. Since this transformation is accompanied by expansion of the rhombohedral unit cell, such volume change ($\Delta V = 11$ Å^3) indicates the first-order character of the structural phase transition.

4.2 | Polar orthorhombic phases of Ln$_2$H$_4$O

4.2.1 | $Pmn2_1$ architecture

The distinctive feature of $Pmn2_1$ structural organization (subjected to point group C_{2v}) is that all atoms occupy the sites distributed on mirror planes. This may allow us to represent the lattice skeleton as an ordered superstructure that is derived from the the ideal wurtz-stannite structure [38] by eliminating $4b$ positions of the pristine unit cell. The search for a prototype phase for the given structure was performed by analyzing the respective displacive transformations obtained by using isomorphism conditions of group-supergroup relations. Our calculations allowed us to attribute

(a) R-$3m$ trigonal structure

(b) $Pmmn$ orthorhombic structure

(c) $Amm2$ orthorhombic structure

(d) $Cmc2_1$ orthorhombic structure

(e) P-$4m2$ tetragonal structure

(f) $P2_1/m$ monoclinic structure
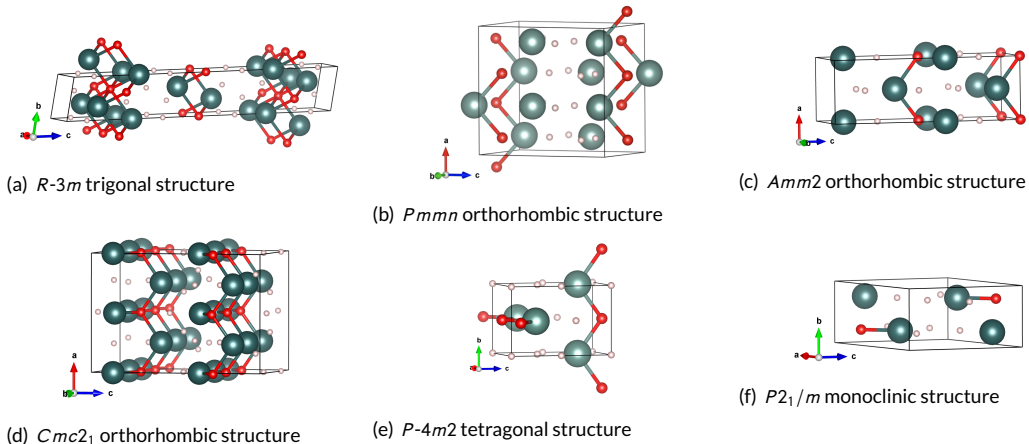
FIGURE 4 Illustrations of the unit cell predicted for the high-symmetry prototype structures of Y$_2$H$_4$O.

the high-symmetry (paraelectric) phase to the centrosymmetric space group $Pmmn$. The crystal unit cell is described in Table 7b and displayed in Figure 4b. Structure instability associated with critical displacements of oxygen and hydrogen sublattices can be related to the displacive mechanism of zone-centered soft modes. The strong purely imaginary amplitude of lowest-lying B_{1u} optical vibrational branch gives rise to lowering the orthorhombic symmetry $Pmmn \rightarrow Pmn2_1$ accompanied by the loss of inversion center. In the low-symmetry polar phase $Pmn2_1$ the spontaneous electrical polarization plays the role of the macroscopic order parameter for the displacive phase transformation.

4.2.2 | $Pmc2_1$ architecture

The next our prediction indicated in Figure 2c relates to crystallization of Ln$_2$H$_4$O into the bulk polar phase associated with the space group $Pmc2_1$. In this lattice geometry, the packing configuration comprises alternating layers of corner-shared LnH$_6$O$_2$ clusters in which the metal cation is located in a distorted decahedral coordination. The ordering is characterized by equal combination of independent eightfold and fourfold Ln coordinations; the former may be decomposed into six-hydrogen-connected nodes and two-oxygen-connected nodes, respectively. From the comparison of hydrogen-oxygen accommodation around Ln positions with the structural characterization of layered perovskites follows that the $Pmc2_1$ lattice can be associated with a distorted form of pseudo-perovskite superstructure. This feature of the perovskite architecture allowed us to easily construct a parent prototype of the $Pmc2_1$ structure. By modeling lattice configurations via isomorphisms of the group-supergroup correspondence we attributed the proper

high-symmetry phase to the non-centrosymmetric polar space group $Amm2$. Table 7c and Figure 4c characterize this base-centered orthorhombic structure. In contrast with the previous case of $Pmn2_1$ symmetry, the nature of structural instability underlying the $Amm2 \rightarrow Pmc2_1$ ferrodistortive transformation turns out to be more complex. Analysis of vibrational and elastic degrees of freedom showed that this symmetry lowering is controlled by the interplay of atomic displacements, polyhedral rotations and spontaneous strains. That is, the overall distortion of the high-symmetry $Amm2$ structure is energetically favorable due two competing factors. First, there occur polar displacements of the ions from their high-symmetric positions within the YH_6O_2 polyhedra; the instability is associated with the critical behaviour of the IR active B_2 soft vibrational modes. Secondly, there occurs a ferroelastic change caused by the e_4 strain contribution to symmetry spontaneous breaking; the instability is associated with the anomalous softness of the elastic constant C_{44}.

4.2.3 | $Pmm2$ architecture

The key feature of geometry with the $Pmm2$ space symmetry is that the mirror planes determine the order of atomic distributions (i.e., all atomic positions occupied in the unit cell have the same C_{2v} point symmetry). The other interesting feature is that no atoms are let into the filling of the $4i$ positions. Due to this fact the system cannot crystallize in high-symmetry hexagonal lattice with $P6mm$ space group and, therefore, reaches the regime of stabilization in the lower-symmetry orthorhombic lattice. The crystal structure of Ln_2H_4O can be considered as a more complex (modified) variant of the dyscrasite (Ag_3Sb) geometry[39]. The modification is connected with the occupation of new oxygen and hydrogen positions which become partially non-uniformly distributed over symmetry-allowed crystallographic sites. Note that such acentric scheme of atomic accommodations is particularly relevant for the ferroelectricity because the macroscopic charge asymmetry is directly induced through the anionic framework. The high-symmetry prototype of the $Pmm2$ phase also is formed within the limits of the orthorhombic geometry: it represents the structure belonged to the $Cmc2_1$ symmetry group (Table 7d and Figure 4d). The $Cmc2_1 \rightarrow Pmm2$ phase transformation occurs by displacive instability which takes place in the basal layers and is accompanied by the transverse shifts of hydrogen atoms; the phase transition can be associated with the condensation of A_2 and B_1 zone-centered soft vibrational modes.

4.3 | Layered phases of Ln_2H_4O with monoclinic distortion

4.3.1 | Pm-type polar architecture with $Z = 1$

This low-symmetry lattice geometry can be attributed to a large distortion of the prototype tetragonal structure determined by the $P\text{-}4m2$ space group. Data on atomic distribution and site symmetry are summarized in Table 7e, the tetragonal unit cell is illustrated in Figure 4e. The ordering in the $P\text{-}4m2$ crystal system of Y_2H_4O can be characterized as being nearly similar to that described by the structure type of ternary intermetallic Zr_2CuSb_3 [40]. Testing of zone-centered harmonic vibrations showed that such $P\text{-}4m2$ lattice geometry is dynamically unstable; the instability takes place at the center of the Brillouin zone and is driven by the imaginary value of lowest E optical mode.

4.3.2 | The effect of stacking: Pm-type polar architecture with $Z = 2$

The addition of structural complexity is accompanied by the appearance of almost double scaling of the lattice parameter a (because of the linkage of admixed layers which doubles the unit cell), and the enlarging of β up to 16 degrees from the initial monoclinic angle (Figure 2f). The crystallographic information on the resulting crystal structure are given in Table S2 of SI. A possible high-symmetry modification of this structure can be represented by centrosymmetric mono-

clinic system with the $P2_1/m$ symmetry (Table 7f). Illustration of the crystal structure is shown in Figure 4f. Particularly relevant for the mechanism of symmetry lowering in the $P2_1/m$ layered geometry are atomic accommodations that are realized through the mirror planes (C_s point symmetry). In such a case, since analysis indicated dynamical stability of the lattice degrees of freedom, the macroscopic charge ordering induced by the structural changes of the $P2_1/m{\rightarrow}Pm$ phase transformation proceeds in a scheme of the reconstructive transition, instead of the displacive mechanism of lattice instability.

4.4 | Off-centering effects of the layered environment

Crystallization of the Ln_2H_4O oxyhydride into lattices of m and $mm2$ classes (Table 1) can be classified under two groups, according the origin of their ferroelectric properties. The first group comprises the Pm (Z=1), $Pmm2$ and $Pmn2_1$ polar phases. The layered structure of materials with Pm and $Pmn2_1$ symmetries offers a simpler interpretation – it can be characterized by the combination of positively (($LnH)^{+2}$) and negatively (($LnH_3O_1)^{-2}$) charged building blocks. Both blocks are key elements of charged layers. To form the bulk structure the layers are stacked in the alternating off-centering order under which the positive layer becomes shifted from the central position and located slightly closer to one of the negative layers. The other structure attribute is that $(LnH)^{+2}$ building blocks form linear chains extended in one direction. In the $Pmm2$ structure, the ordering is modified by addition of the building block $(LnH)^{+2}$ to the negatively charged block $(LnH_3O_2)^{-4}$; their interaction provides formation of two atomic layers $(LnH_2O)^{-1}$. To satisfy the electroneutrality condition, in the remaining part of the $(LnH)^{+2}$ blocks, each block acquires one electron and, accordingly, gives rise to generation of two positively charged layers $(LnH_2)^{+1}$. Results of lattice relaxations showed that the average off-centering of the basic layers in the z-direction can be characterized by the value 0.15 Å for Y_2H_4O and 0.19 Å for La_2H_4O. The one exception relates to the Pm monoclinic phase (with Z=1) of Y_2H_4O where the anomalous displacement of 0.34 Å was evaluated. On the other hand, this feature is not characteristic for the same structure of La_2H_4O. Note also that both these facts are well consistent with the large value of spontaneous polarization predicted for Y_2H_4O (Table 3). The layred structures with Pm (Z=2), $Pmc2_1$ and $Pmn2_1$ symmetries belong to the other group. All of them can be described in terms of LnH_3 and $LnHO$ building blocks those combinations form alternating layers stacked along the principal z-axis. Characteristic feature is that a macroscopic configuration of $Ln-O$ bonds arranges in such an order as to be also oriented along one direction.

4.5 | Modeling, computational details, and post-processing analysis

Guide on compositional and structural modeling of ternary yttrium oxyhydrides has been presented in our previous studies [13, 14]. Electron structure calculations were performed within the numerical framework of density functional theory (DFT) by using Vienna ab initio simulation package (VASP) [41]. The Perdew-Burke-Ernzerhof (PBE) GGA exchange-correlation functional[43] was employed to determine the Kohn-Sham one-electron eigenstates and energies. The potential projector augmented-wave method[44, 45] (PAW) employed the PAW-PBE pseudo-potentials with the plane-wave basis sets of $4s^24p^65s^24d^1$, $2s^22p^4$, and $1s^1$ valence electron configurations for Y, O, and H elements, respectively. By taking plane-wave energy cutoffs of 700 eV and $8 \times 8 \times 8$ Γ-centered **k**-mesh for the reciprocal-space integration over the Brillouin zone we obtained the well-converged results of periodic calculations with the degree of accuracy below 1 meV/(unit cell). The equilibrium lattice structures were fully optimized with respect to unit cell constants and internal atom positions. For yttrium containing systems the simulations have been conducted with the PBE-GGA functional, while to account for strong on-site correlations in La_2H_4O we used the Dudarev scheme [46] of GGA + U implementation. According to Ref. [47], the U_{eff} parameter of 5.5 eV takes into account the Hubbard correction

associated with the atomic $4f$ shell of the lanthanum ion. Analysis of the elastic properties was performed on the base of the ELATE online tool [48, 49]. Aggregate properties of the crystal phases of Table 1 have been evaluated in the Hill approximation [50]. The Grüneisen parameter (γ) and the Debye temperature (Θ_D) have been calculated according to semi-empirical approaches of Refs. [51] and [52], respectively. Estimates of the Vickers hardness H_V have been obtained from the model relations of Refs. [53, 54]. The dielectric and piezoelectric properties have been simulated by using numerical procedures of density functional perturbation theory[55]. The theory-group analysis was performed by means of the program tools[56] hosted by Bilbao Crystallographic Server[58, 59]. The ISOTROPY software suite[62, 63], and the VESTA program[64] have been used for characterization of the crystal structures. The formation energy (the heat of formation at T = 0 K) was estimated as the difference between the total energy per formula unit and the sum of the energies of constituent elements. The spontaneous electric polarization was evaluated by using the Berry phase method [65] as implemented in VASP. Based on relaxed lattice geometries, ionic and electronic contributions to total macroscopic polarization were calculated in terms of differences of the corresponding dipole moments for symmetry-allowed directions with respect to distorted and undistorted structures. Determination of the polarization character (ferroelectric or pyroelectric order) was made through the comparison of total energy calculations with respect to a reversion of the total polarization.

SUPPORTING INFORMATION

Data details on material properties are presented in Supporting Information.

ACKNOWLEDGEMENTS

CONFLICT OF INTEREST

The authors declare no conflict of interest.

REFERENCES

[1] Hayward MA, Cussen EJ, Claridge JB, Bieringer M, Rosseinsky MJ, Kiely CJ, et al. The Hydride Anion in an Extended Transition Metal Oxide Array: LaSrCoO$_3$H$_{0.7}$. Science 2002;295(5561):1882–1884. `http://science.sciencemag.org/content/295/5561/1882`.

[2] Helps RM, Rees NH, Hayward MA. Sr$_3$Co$_2$O$_{4.33}$H$_{0.84}$: An Extended Transition Metal Oxide-Hydride. Inorg Chem 2010;49(23):11062–11068. `https://doi.org/10.1021/ic101613b`, pMID: 21033678.

[3] Yamamoto T, Kageyama H. Hydride Reductions of Transition Metal Oxides. Chem Lett 2013;42(9):946–953. `https://doi.org/10.1246/cl.130581`.

[4] Kobayashi Y, Hernandez O, Tassel C, Kageyama H. New chemistry of transition metal oxyhydrides. Chem LettSci Technol Adv Mater 2017;18(1):905–918. `https://doi.org/10.1080/14686996.2017.1394776`, pMID: 29383042.

[5] Fokin VN, Malov YI, Fokina EE, Troitskaya SL, Shilkin SP. Investigation of interactions in the TiH$_2$-O$_2$ system. Int J Hydrogen Energy 1995;20(5):387 – 389. `http://www.sciencedirect.com/science/article/pii/036031999400075B`.

[6] Fokin VN, Malov YI, Fokina EE, Shilkin SP. Study of the phase-forming features in the ZrH$_2$-O$_2$ system. Int J Hydrogen Energy 1996 11;21:969–973.

[7] Fokin VN, Fokina EE, Shilkin SP. Oxidation of Metal Hydrides with Molecular Oxygen. Russ J Gen Chem 2004 Apr;74(4):489–494. `https://doi.org/10.1023/b:rugc.0000031845.00588.d0`.

[8] Mongstad T, Platzer-Björkman C, Maehlen JP, Mooij LPA, Pivak Y, Dam B, et al. A new thin film photochromic material: Oxygen-containing yttrium hydride. Sol Energy Mater Sol Cells 2011;95(12):3596 – 3599. `http://www.sciencedirect.com/science/article/pii/S0927024811004764`.

[9] Montero J, Martinsen FA, García-Tecedor M, Karazhanov SZ, Maestre D, Hauback B, et al. Photochromic mechanism in oxygen-containing yttrium hydride thin films: An optical perspective. Phys Rev B 2017 May;95:201301. `https://link.aps.org/doi/10.1103/PhysRevB.95.201301`.

[10] La M, Li N, Sha R, Bao S, Jin P. Excellent photochromic properties of an oxygen-containing yttrium hydride coated with tungsten oxide (YH$_x$:O/WO$_3$). Scr Mater 2018;142:36 – 40. `http://www.sciencedirect.com/science/article/pii/S1359646217304748`.

[11] Nafezarefi F, Schreuders H, Dam B, Cornelius S. Photochromism of rare-earth metal-oxy-hydrides. Appl Phys Lett 2017;111(10):103903. `https://doi.org/10.1063/1.4995081`.

[12] Pishtshev A, Karazhanov SZ. Role of oxygen in materials properties of yttrium trihydride. Solid State Commun 2014;194:39 – 42. `http://www.sciencedirect.com/science/article/pii/S0038109814002671`.

[13] Pishtshev A, Strugovshchikov E, Karazhanov S. Conceptual Design of Yttrium Oxyhydrides: Phase Diagram, Structure, and Properties. Cryst Growth Des 2019;19(5):2574–2582. `https://doi.org/10.1021/acs.cgd.8b01596`.

[14] Pishtshev A, Strugovshchikov E, Karazhanov S, Two Faces of Hydrogen in Yttrium Hydroxyhydride: Y$_2$H$_3$O(OH) – a New Inorganic Chiral System with Hydridic and Protonic Hydrogens. American Chemical Society (ACS); 2018. `https://doi.org/10.26434/chemrxiv.6301571.v1`.

[15] Lappe F, Niggli A, Nitsche R, White JG. The crystal structure of In$_2$ZnS$_4$. Z Kristallogr 1962 aug;117(2-3):146–152. `https://doi.org/10.1524/zkri.1962.117.2-3.146`.

[16] Berand N, Range KJ. A redetermination of the crystal structure of the (III)a-polytypic form of diindium zinc tetrasulfide, ZnIn2S4. J Alloys Compd 1994 mar;205(1-2):295–301. `https://doi.org/10.1016/0925-8388(94)90805-2`.

[17] Strugovshchikov E, Pishtshev A, Optical properties of polar phases of Ln$_2$H$_4$O (Ln=Y, La) (to be published); 2019.

[18] Heyd J, Scuseria GE, Ernzerhof M. Hybrid functionals based on a screened Coulomb potential. J Chem Phys 2006 01;124:8207–8215.

[19] V Krukau A, A Vydrov O, F Izmaylov A, E Scuseria G. Influence of the Exchange Screening Parameter on the Performance of Screened Hybrid Functional. J Chem Phys 2007 01;125:224106.

[20] Kidyarov BI. Comparative Interrelationship of the Structural, Nonlinear-Optical and Other Acentric Properties for Oxide, Borate and Carbonate Crystals. Crystals 2017;7(4). `https://www.mdpi.com/2073-4352/7/4/109`.

[21] Ren B, Or SW, Zhang Y, Zhang Q, Li X, Jiao J, et al. Piezoelectric energy harvesting using shear mode 0.71Pb(Mg$_{1/3}$Nb$_{2/3}$)O$_3$-0.29PbTiO$_3$ single crystal cantilever. Appl Phys Lett 2010 Feb;96(8):083502.

[22] Zeng Z, Ren B, Gai L, Zhao X, Luo H, Wang D. Shear-Mode-Based Cantilever Driving Low-Frequency Piezoelectric Energy Harvester Using 0.67Pb(Mg1/3Nb2/3)O3-0.33PbTiO3. IEEE Trans Sonics Ultrason 2016 05;63:1–1.

[23] Topolov VY, Bisegna P, Bowen CR. Piezo-Active Composites: Orientation Effects and Anisotropy Factors. Springer Series in Materials Science, Springer Berlin Heidelberg; 2013.

[24] De Jong M, Chen W, Geerlings H, Asta M, Persson K. A database to enable discovery and design of piezoelectric materials. Sci Data 2015 09;2:150053.

[25] Caliò R, Rongala U, Camboni D, Milazzo M, Stefanini C, De Petris G, et al. Piezoelectric Energy Harvesting Solutions. Sensors 2014 03;14:4755–90.

[26] Yu X, Hou Y, Zhao H, Fu J, Zheng M, Zhu M. The role of secondary phase in enhancing transduction coefficient of piezoelectric energy harvesting composites. J Mater Chem C 2019 02;7.

[27] Gao J, Xue D, Liu W, Zhou C, Ren X. Recent Progress on BaTiO3-Based Piezoelectric Ceramics for Actuator Applications. Actuators 2017;6(3). https://www.mdpi.com/2076-0825/6/3/24.

[28] Wang P, Du H, Shen S, Zhang M, Liu B. Deposition, characterization and optimization of zinc oxide thin film for piezoelectric cantilevers. Appl Surf Sci 2012;258(24):9510 – 9517. http://www.sciencedirect.com/science/article/pii/S0169433212008124.

[29] Lu Y, Emanetoglu NW, Chen Y. Chapter 13 - ZnO Piezoelectric Devices. In: Jagadish C, Pearton S, editors. Zinc Oxide Bulk, Thin Films and Nanostructures Oxford: Elsevier Science Ltd; 2006.p. 443 – 489. http://www.sciencedirect.com/science/article/pii/B9780080447223500130.

[30] Malakooti M, Sodano H. Piezoelectric energy harvesting through shear mode operation. Smart Mater Struct 2015 05;24.

[31] Uchino K. Glory of piezoelectric perovskites. Chem LettSci Technol Adv Mater 2015;16(4):046001. https://doi.org/10.1088/1468-6996/16/4/046001.

[32] Pishtshev A. Electron-TO-phonon interaction in polar crystals. Phys B 2011;406(8):1586–1591.

[33] Davis M, Budimir M, Damjanovic D, Setter N. Rotator and extender ferroelectrics: Importance of the shear coefficient to the piezoelectric properties of domain-engineered crystals and ceramics. J Appl Phys 2007;101(5):054112. https://doi.org/10.1063/1.2653925.

[34] Aoki T, Umemiya S, Hida M, Kurihara K. Measurement of d_{15} Shear-Mode Piezoelectric Response in PZT Thin Film. Key Eng Mater 2009 12;421-422:95–98.

[35] Nakamura K. 17 - Ultrasonic motors. In: Gallego-Juárez JA, Graff KF, editors. Power Ultrasonics Oxford: Woodhead Publishing; 2015.p. 511 – 541. http://www.sciencedirect.com/science/article/pii/B978178242028600017X.

[36] Maurya D, Yan Y, Priya SJ. In: Piezoelectric Materials for Energy Harvesting; 2015. p. 143–178.

[37] Du XH, Belegundu U, Uchino K. Crystal Orientation Dependence of Piezoelectric Properties in Lead Zirconate Titanate: Theoretical Expectation for Thin Films. Jpn J Appl Phys 1997 09;36:5580–5587.

[38] Wold A, Dwight K. Solid State Chemistry: Synthesis, Structure, and Properties of Selected Oxides and Sulfides. Springer Netherlands; 1993.

[39] Villars P, Cenzual K, editors, Ag_3Sb Crystal Structure: Datasheet from "PAULING FILE Multinaries Edition – 2012" in SpringerMaterials. Springer-Verlag Berlin Heidelberg & Material Phases Data System (MPDS), Switzerland & National Institute for Materials Science (NIMS), Japan; 2012. https://materials.springer.com/isp/crystallographic/docs/sd_0261320, copyright 2016 Springer-Verlag Berlin Heidelberg & Material Phases Data System (MPDS), Switzerland & National Institute for Materials Science (NIMS), Japan.

[40] Koblyuk N, Melnyk G, Romaka L, Bodak OI, Fruchart D. Crystal structure of Zr_2CuSb_3 and related compounds. J Alloys Compd 2001;317-318:284 – 286. http://www.sciencedirect.com/science/article/pii/S0925838800013499, the 13th International Conference on Solid Compounds of Transition Elements.

[41] Kresse G, Furthmüller J. Efficiency of ab-initio total energy calculations for metals and semiconductors using a plane-wave basis set. Comput Mater Sci 1996;6(1):15–50.

[42] Kresse G, Furthmüller J. Efficient iterative schemes for *ab initio* total-energy calculations using a plane-wave basis set. Phys Rev B 1996 Oct;54:11169–11186.

[43] Perdew JP, Burke K, Ernzerhof M. Generalized Gradient Approximation Made Simple. Phys Rev Lett 1996;77(18):3865–3868.

[44] Blöchl PE. Projector augmented-wave method. Phys Rev B 1994 Dec;50:17953–17979.

[45] Kresse G, Joubert D. From ultrasoft pseudopotentials to the projector augmented-wave method. Phys Rev B 1999 Jan;59:1758–1775.

[46] Dudarev SL, Botton GA, Savrasov SY, Humphreys CJ, Sutton AP. Electron-energy-loss spectra and the structural stability of nickel oxide: An LSDA+U study. Phys Rev B 1998 Jan;57:1505–1509. `https://link.aps.org/doi/10.1103/PhysRevB.57.1505`.

[47] Topsakal M, Wentzcovitch R. Accurate projected augmented wave (PAW) datasets for rare-earth elements (RE=La-Lu). Comput Mater Sci 2014 08;95.

[48] Gaillac R, Pullumbi P, Coudert FX. ELATE: an open-source online application for analysis and visualization of elastic tensors. J Phys: Condens Matter 2016;28(27):275201. `http://stacks.iop.org/0953-8984/28/i=27/a=275201`.

[49] Gaillac R, Coudert FX, ELATE: Elastic tensor analysis;. `http://progs.coudert.name/elate`.

[50] Hill R. The Elastic Behaviour of a Crystalline Aggregate. Proc Phys Soc, London, Sect A 1952;65(5):349. `http://stacks.iop.org/0370-1298/65/i=5/a=307`.

[51] Belomestnykh VN, Tesleva EP. Interrelation between anharmonicity and lateral strain in quasi-isotropic polycrystalline solids. Tech Phys 2004 Aug;49(8):1098–1100. `https://doi.org/10.1134/1.1787679`.

[52] Anderson OL. A simplified method for calculating the debye temperature from elastic constants. J Phys Chem Solids 1963;24(7):909 – 917. `http://www.sciencedirect.com/science/article/pii/0022369763900672`.

[53] Chen XQ, Niu H, Li D, Li Y. Modeling hardness of polycrystalline materials and bulk metallic glasses. Intermetallics 2011;19(9):1275 – 1281. `http://www.sciencedirect.com/science/article/pii/S0966979511000987`.

[54] Tian Y, Xu B, Zhao Z. Microscopic theory of hardness and design of novel superhard crystals. Int J Refract Met Hard Mater 2012;33:93 – 106. `http://www.sciencedirect.com/science/article/pii/S026343681200042X`.

[55] Gajdoš M, Hummer K, Kresse G, Furthmüller J, Bechstedt F. Linear optical properties in the projector-augmented wave methodology. Phys Rev B 2006 Jan;73:045112. `https://link.aps.org/doi/10.1103/PhysRevB.73.045112`.

[56] Ivantchev S, Kroumova E, Madariaga G, Pérez-Mato JM, Aroyo MI. *SUBGROUPGRAPH*: a computer program for analysis of group–subgroup relations between space groups. J Appl Crystallogr 2000;33(4):1190–1191.

[57] Kroumova E, Aroyo MI, Pérez-Mato JM, Kirov A, Capillas C, Ivantchev S, et al. Bilbao Crystallographic Server I: Databases and crystallographic computing programs. Phase Transitions 2003;76:155–170.

[58] Bilbao Crystallographic Server;. `http://www.cryst.ehu.es`.

[59] Aroyo MI, Pérez-Mato JM, Orobengoa D, Tasci ES, de la Flor G, Kirov A. Crystallography online: Bilbao Crystallographic Server. Bulg Chem Commun 2011;43(2):183–197.

[60] Aroyo MI, Pérez-Mato JM, Capillas C, Kroumova E, Ivantchev S, Madariaga G, et al. Bilbao Crystallographic Server I: Databases and crystallographic computing programs. Z Krist 2006;221(1):15–27.

[61] Aroyo MI, Kirov A, Capillas C, Pérez-Mato JM, Wondratschek H. Bilbao Crystallographic Server. II. Representations of crystallographic point groups and space groups. Acta Cryst 2006;A62(2):115–128.

[62] Stokes HT, Hatch DM, Campbell BJ, ISOTROPY Software Suite;. http://stokes.byu.edu/iso/isotropy.php.

[63] Stokes HT, Hatch DM. *FINDSYM*: program for identifying the space-group symmetry of a crystal. J Appl Crystallogr 2005 Feb;38(1):237–238. http://dx.doi.org/10.1107/S0021889804031528.

[64] Momma K, Izumi F. *VESTA3* for three-dimensional visualization of crystal, volumetric and morphology data. J Appl Crystallogr 2011 Dec;44(6):1272–1276.

[65] Resta R, Vanderbilt D. Theory of Polarization: A Modern Approach. In: Physics of Ferroelectrics: A Modern Perspective Springer Berlin Heidelberg; 2007.p. 31–68. https://doi.org/10.1007/978-3-540-34591-6_2.